

Volume 2, Issue 4, 2012, 380-391

Received: 11.07.2012 / Accepted: 26.07.2012 / Published on-line: 14.08.2012

Bio-inspired mineralization of zinc oxide in presence of ZnO-binding peptides**Johannes Baier^{1*}, Torsten Naumburg¹, Nina J. Blumenstein¹, Lars P. H. Jeurgens², Udo Welzel², Tuan A. Do³, Jürgen Pleiss³, and Joachim Bill¹****ABSTRACT**

Dissolved peptides have a substantial influence on the zinc oxide (ZnO) morphology during bio-inspired precipitation at near-neutral pH and 37 °C. The influences of three different ZnO-binding peptides were investigated, which have isoelectric points in the acidic, near neutral and basic pH range, respectively. It can be shown, that (1) the peptides inhibit the crystal growth of ZnO crystals by selective adsorption on the surfaces. (2) Ostwald rule of stages is the key for understanding the precipitation mechanism under bio-inspired conditions and (3) layered basic zinc salts (LBZs) are metastable phases within the precipitation mechanism.

Keywords: *ZnO, peptide, bio-inspired, mineralization, layered basic zinc salts, intercalation, Ostwald rule of stages*

1. INTRODUCTION

Due to their broad application possibilities, zinc oxide (ZnO) and layered basic zinc salts (LBZs) are considered as attractive candidates for the development of novel nanomaterial-based technologies. For example, ZnO plays an important role as a semiconductor, which offers applications in liquid crystal displays, solar cells, blue-light emitting diodes (LEDs) and transistors [1–5]. Furthermore, ZnO can also be used as an inert additive to improve mechanical properties. LBZs are of great interest, because of their utility as an anion-exchanger [6–10] or as a catalyst [11]. The reported exchange properties can be described with the general formula $[(\text{Zn}^{\text{octa}})_3(\text{Zn}^{\text{tetra}})_2(\text{OH})_8]^{2+} \cdot 2(\text{A}^-) \cdot n\text{H}_2\text{O}$, in which the anion A^- can be replaced by other anions. The exchange of the intercalated anions can expand or contract the dimension along the basal axis (Table 1), while the general structure is maintained.

Since the requirements imposed on the material can often be achieved only by hard synthesis conditions, it is important to investigate new synthesis strategies. In fact, the bio-inspired approach allows the synthesis under mild conditions, which additionally lowers the energy consumption and production costs. Numerous publications deal with the influence of peptides and proteins on the formation of ZnO and LBZs under moderate conditions [12–22]. Gerstel et al. [13] investigated the effect of amino acids and dipeptides on crystal size and morphology of the precipitates from a zinc nitrate precursor solution. In total, the influence of eight amino acids and 21 dipeptides was systematically analyzed. Various functional and structured ZnO-based materials with a large variety of geometries were also generated. In the case of ZnO materials, molecular modeling has also been

¹ Institute for Materials Science, University of Stuttgart, Stuttgart

*Corresponding author e-mail address: baier@imw.uni-stuttgart.de

² Max Planck Institute for Intelligent Systems, Stuttgart

³ Institute for Technical Biochemistry, University of Stuttgart, Stuttgart

made to determine how small organic molecules interact with the ZnO surfaces using molecular dynamics (MD) simulation [23–25]. Recently, MD simulation *in vacuo* was applied to model the

Table 1: Basal parameters calculated from the X-ray diffraction patterns of different LBZs.

Anion	Basal distance (reflection used) [Å]	Interlayer distance [Å] ^a	Lit.
Nitrate	9.89	5.11	9
Succinate	12.2	7.4	7
Glutarate	13.2	8.3	7
Adipate	14.49	9.71	9
Adipate	14.5	9.7	7
Terephthalate	14.5	9.7	6
Azelate	16.27	11.49	9
Benzoate	19.0	14.2	7
Benzoate	19.10	14.32	9
Benzoate	19.3	14.5	6
I3A ^b	23.5	18.7	41
DPBA ^c	29.6	24.8	42

^a Calculated by subtracting the brucite layer thickness from the basal distance (4.78 Å, JCPDS card 44-1482); ^b Indole-3-acetate; ^c 4-(2,4-dichlorophenoxy)butyrate.

Table 2: Parameters of selected peptides [26].

Peptide	Sequence	pI ^a
31	HHGHSPTSPQVR	9.77
07	LLADTTHHRPWT	6.92
46	ERSWTLDSALSM	4.37

^a Calculated isoelectric points (pI) (Vector NTI software, Invitrogen).

interactions of peptides with a ZnO surface and to evaluate the adsorption energies in order to identify the molecular basis of their inhibition effects on the ZnO particle growth. Based on these studies we investigated the bio-inspired precipitation of ZnO in presence of ZnO-binding 12-mer peptides, which have previously been identified by phage-display experiments. The results of corresponding phage-display experiments have been published elsewhere [26]. To study the precipitation mechanism, we selected three peptides from the phage library with isoelectric points (pI) in the acidic, near-neutral and basic pH range, respectively (Table 2). Peptide binding to ZnO was modelled by extensive molecular dynamics simulations in explicit water and the binding free energy was determined. By combining simulation results with experimental data, we expected to gain more valuable insights into the peptide-mediated precipitation of ZnO.

2. EXPERIMENTAL SECTION

An aqueous buffer solution of 30 mM tris(hydroxymethyl)-aminomethane (Trizma) at about pH 8 was prepared by dissolving 1.842 g l⁻¹ Trizma hydrochloride and 2.22 g l⁻¹ Trizma base in deionized water. The peptides and their sequences used in this work are presented in Table 2. They were dissolved with a final concentration of 0.5 or 1.0 mg ml⁻¹ in this buffer. The reaction was started by adding a 500 mM Zn(NO₃)₂ · 6H₂O solution to achieve final concentrations of 20 mM Zn²⁺ in the peptide-buffer solution. The reactions were performed in an oven (37 °C). Reactions were stopped after 4 h and 6 weeks. Due to strong charging and decomposition effects under X-ray irradiation, the XPS measurement with peptide 31 was made with a precipitate, which was prepared in a buffered solution at pH 7.5 (adjusted with NaOH solution). The precipitation time was 4.5 h in this experiment. All precipitates were centrifuged and dried at 37 °C in air.

2.1. Powder X-ray Diffraction (XRD). The XRD patterns were recorded with a Siemens D5000 diffractometer in Bragg-Brentano geometry, using a Cu K α radiation (30 mA and 40 kV) in a 2 Θ range of 2° to 60° with a step size of 0.02° and a scan rate of 0.25° min⁻¹. In a few cases, XRD

data were recorded with an X'Pert MPD diffractometer (Panalytical). Measurements were made in Bragg-Brentano geometry, using Cu $K\alpha_1$ radiation (X-ray tubes setting of 30 mA and 40 kV) employing a primary-beam Johansson monochromator in a 2Θ range of 3° to 60° . A position-sensitive detector (X'Celerator, Panalytical) was employed.

For line-broadening analysis, the reflections with a sufficiently high peak-to-background ratio in the diffraction angle range between about 30° and 60° (pertaining to the ZnO (100), (002), (101), (102) and (110) reflections) were investigated. Peak-maximum positions, full widths at half maximum (FWHM), integral breadths and integrated intensities were determined by fitting Pearson VII functions to the measured diffraction lines. The line broadening was analyzed on the basis of the single-line method by attributing Lorentzian line broadening to crystallite size and Gaussian line broadening to microstrain [27,28]. A correction for instrumental broadening was done on the basis of reference measurements employing a powder layer of LaB_6 (Standard Reference Material SRM 660a, National Institute of Standard and Technology NIST, Gaithersburg, USA) deposited by sedimentation on a zero-background specimen holder using a Voigt-function approach to subtract instrumental broadening [27].

2.2. Scanning Electron Microscopy (SEM). Micrographs were taken with a DSM 982 Gemini (Zeiss). An accelerating voltage of 2–3 kV and a working distance of 3–5 mm were used.

2.3. Fourier Transform Infrared Spectroscopy (FTIR). The FTIR experiments were performed by an IFS 66 Spectrometer (Bruker). Precipitates were mixed with KBr and compacted to pellets. The spectra were recorded from 4000 to 400 cm^{-1} .

2.4. Thermogravimetry (TG). The mass loss of precipitates upon heating was monitored by thermogravimetry by using a STA 409 (Netzsch). The synthesized composites were heated, analog to Bauermann et al. [16] up to 850°C with a heating rate of 10 K min^{-1} .

2.5. X-ray Photoelectron Spectroscopy (XPS). The XPS analysis was performed using a Thermo VG Thetaprobe system employing monochromatic Al- $K\alpha$ radiation ($h\nu=1486.68\text{ eV}$; spot size of $400\text{ }\mu\text{m}$), while operating the radian analyser in the so-called 'standard' lens mode by simultaneously collecting all photoelectrons over the detection angle range between 23° and 83° (with respect to the specimen surface normal; i.e. the central detection angle equals 53°) [29]. XPS survey spectra, covering a binding energy (BE) range from 0 eV to 1200 eV, were recorded with a step size and constant pass energy of 0.2 eV and of 200 eV, respectively. Detailed XPS spectra of the Zn $2p_{3/2}$ - Zn $2p_{1/2}$ doublet, O 1s, N 1s and C 1s regions were recorded with a step size and constant pass energy of 0.05 eV and 50 eV, respectively. The energy scale of the hemispherical analyser was calibrated by referencing the Au $4f_{7/2}$, Ag $3d_{5/2}$ and Cu $2p_{3/2}$ main peaks (as measured *in situ* for corresponding sputter-cleaned, high-purity metal references) to the recommended BE positions of 83.96 eV, 368.21 eV and 932.62 eV, respectively. Spectral reconstruction of each region was performed by subtraction of a Shirley-type inelastic background over the concerned binding energy (BE) range for each spectral region, and subsequent, constrained, linear-least-squares fitting with one or more symmetric (mixed Gaussian-Lorentzian) peak components (while taking the same Gaussian-Lorentzian fraction and full width at half-maximum (FWHM) for each component in the fitted spectrum). Finally, the BE scales of the fitted spectral regions were aligned (thereby correcting for possible differential charging effects) by shifting each BE scale according to the averaged BE difference between the resolved Zn $2p_{3/2}$ main peak at the higher BE side of the Zn $2p_{3/2}$ peak envelope and the corresponding reference BE value of 1021.9 eV for ZnO (as determined for a ZnO reference sample in the present study).

2.6. Molecular modeling. The binding free energy of peptide 31, peptide 07, and peptide 46 upon binding to the polar ZnO (001) and nonpolar ZnO (100)-surfaces was modeled using MD simulations at constant temperature (300 K) and constant pressure (1 bar) using the simulation package GROMACS 4.5.3 [30]. For the peptide the AMBER force field [31,32] was used with the N-terminus, histidines, lysines, and arginines protonated, C-terminus, aspartic and glutamic acids deprotonated. For water the TIP3P model was used [31]. The ZnO slab was modeled based on a wurtzite crystal structure [33]. To reduce the dipole moment of the polar (001)-surface, 25% of the negatively charged oxygen atoms on the O-terminated side and 25% of the positively charged zinc atoms on the Zn-terminated side were removed [23]. The peptides were equilibrated for 5 ns in explicit water at a distance of 6 nm from the ZnO surface and then pulled towards the ZnO surfaces with a decreasing pull velocity from 0.5 to 0.1 nm ns⁻¹ and a force constant of 3000 kJ mol⁻¹ nm⁻² during a 15–20 ns steered MD simulation. When a peptide contacted the ZnO surface, the peptide was simulated for 5 ns without external forces to reach an equilibrium state for the system. The peptide conformation at the end of this equilibration time was used as initial conformation for a steered MD simulation along a pathway perpendicular to the ZnO surface and a pull velocity of 0.5 nm ns⁻¹ to model the desorption. For each peptide, 3 adsorption-equilibration-desorption simulations were performed. For each desorption trajectory, a series of umbrella sampling simulations was performed to evaluate the potential of mean force (PMF). At least 25–35 conformers along the desorption trajectory were selected resulting in a window spacing of 0.1–0.12 nm (center of mass separation). For each conformer a 5 ns MD simulation with constraint center of mass was performed. The windows were combined using the weighted histogram analysis method (WHAM [34]) to compute the unbiased distribution and the associated PMF.

3. RESULTS SECTION

The short-term experiments at 37 °C were carried out with all three chosen peptides (peptide 31, peptide 07 and peptide 46). The precipitates were analyzed with FTIR, TG, XRD and XPS.

Representative FTIR spectra of the precipitates are shown in Figure 1, which demonstrate the presence of the peptides. At about 1650 cm⁻¹ there is the absorption band of amid I, which can be correlated to the characteristic vibration of the C=O stretching of peptides [35,36]. The band at 1540 cm⁻¹ corresponds to the typical N-H deformation of amide II vibration [35].

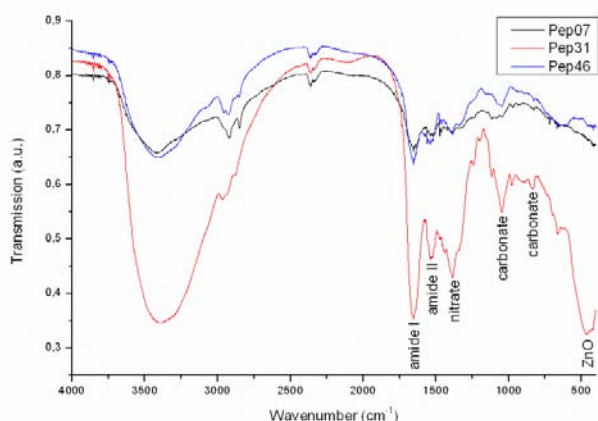


Figure 1: Room temperature FTIR spectra of the as-synthesized ZnO-peptide composites (Deposition time: 4 h).

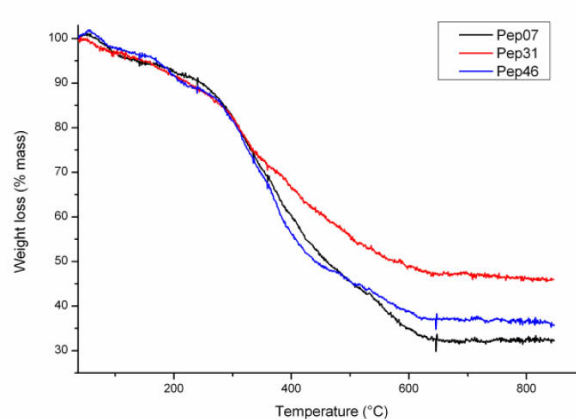


Figure 2: Thermogravimetric measurements of the as-synthesized ZnO-peptide composites (Deposition time: 4 h) by heating in air up to 850 °C using a heating rate of 10 K min⁻¹.

The sharp band at 1385 cm^{-1} is attributed to the nitrate anion, coming from excess zinc nitrate solution. There are also two additional bands at about 1040 cm^{-1} and 840 cm^{-1} , which can be attributed to ν_1 (A_1') symmetric stretching mode and ν_2 (A_2'') out-of-plane bending mode of carbonate [37,38]. This anion is an impurity coming from atmospheric carbon dioxide. In presence of peptide 31 the ZnO band can also be detected at about 470 cm^{-1} . In the latter case the bands are more intensive due to the higher amount of precipitate that was used for the analysis.

The weight losses of the short-term precipitates were measured by thermogravimetric experiments while raising the temperature up to $850\text{ }^\circ\text{C}$ (Figure 2). There is a similarity in the temperature range from $37\text{ }^\circ\text{C}$ up to $300\text{ }^\circ\text{C}$. The weight loss of the precipitates is completed near $600\text{ }^\circ\text{C}$, which is in agreement with the decomposition behaviour of different ZnO-protein composites [16]. The relatively low weight loss in the case of peptide 31 is due to the fact that the positively charged peptide cannot intercalate within the LBZs structure. Thus the identified peptide within IR spectrum might be a result of a small amount of adsorbed molecules (cf. Figure 1).

The XRD patterns of the precipitate containing peptide 31, which has the highest isoelectric point (9.8), suggest the presence of a LBZs. Figure 3 shows a strong reflection at about 9.1° (9.7 \AA), which can be correlated to the nitrate containing LBZs [6]. The second proximate basal spacing of the first reflection could be a result of different amounts of water molecules within the interlayer space [13,39]. Due to the high pI the cationic charged peptide 31 cannot intercalate between the also positively charged hydroxidic layers of LBZs. The detected peptide in the corresponding FTIR spectrum is a result of excess peptide within solution. Furthermore the broad reflection at about 12.0° (7.4 \AA) is in the range of the metastable α -hydroxide of zinc [40]. Please note, that no reflections of zinc oxide can be detected within the XRD diagram, whereas ZnO is present in the FTIR spectrum (cf. Figure 1). This can be a result of different sensitivities of both methods. In the case of the two other peptides the typical reflexions of zinc oxide are present. This is in accordance with the lower isoelectric points of these peptides, resulting in a negative net charge of the molecules. Additionally, the α -hydroxide of zinc can be identified as well as the LBZs: The low diffraction angles (corresponding to large interlayer distances) indicate that the anionic peptides are intercalated between the hydroxidic layers.

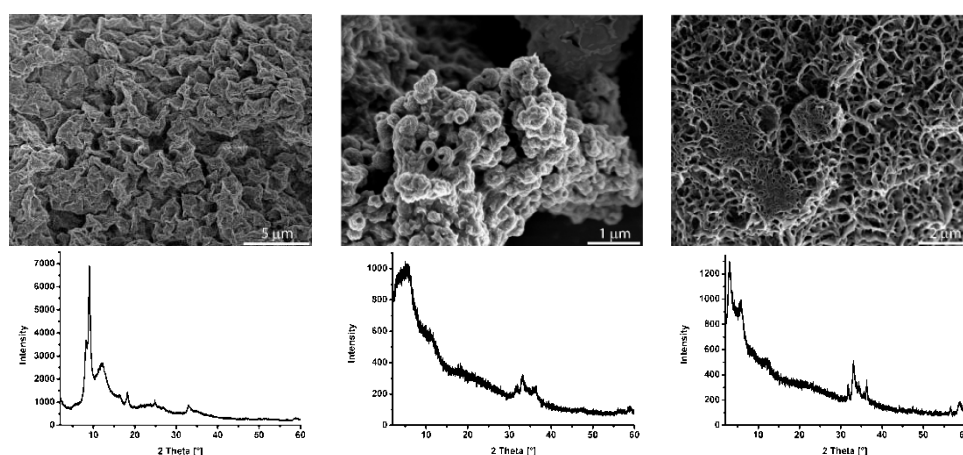


Figure 3: XRD diagrams and SEM figures of short-term experiments (4 h) with peptide 31, peptide 07 and peptide 46 (from left to right).

The measured values of 5.1° (17.2 \AA) for peptide 07 and 5.9° (15.1 \AA) for peptide 46, respectively, are in good agreement with other LBZs containing large anions (cf. Table 1). In the case of peptide 46 there is also an additional reflection at 3.3° (27.1 \AA), which can be explained by a double anionic

layer of the peptide. The same phenomenon of an organic double layer is also known from other anions, e. g. Benzoate [6,7,9], indole-3-acetate [41] or 4-(2,4-dichlorophenoxy)butyrate [42].

There is also one characteristic broad reflection at about 33.2° (2.7 \AA) in the XRD diagrams originating from the layered zinc hydroxide $[\text{Zn}_5(\text{OH})_6(\text{CO}_3)_2]$ (powder diffraction file (PDF) 19-1458) [43,44]. It is well known, that carbonate anions are readily intercalated within the interlayers of LBZs and layered double hydroxides [6,40,45,46]. This result is also consistent with FTIR measurements, which have confirmed the presence of carbonate anions within the precipitate. In the XRD pattern, the intensity of the (200)-reflection of the leaf like $[\text{Zn}_5(\text{OH})_6(\text{CO}_3)_2]$ particles at about 13° is nearly suppressed, indicating an orientation of agglomerates on the substrate surface [43].

The chemical constitutions of the precipitates (and of a ZnO reference sample) were investigated by XPS. The BE values of the Zn $2p_{3/2}$, O 1s, N 1s and C 1s main peaks, as resolved by constrained fitting of the charge-corrected spectra, are reported in Tables 3 and 4 (*note*: the BE scales of the measured XPS spectra were referenced in respect to the Zn $2p_{3/2}$ main peak of the ZnO reference positioned at $1021.9 \pm 0.1 \text{ eV}$; see experimental XPS section).

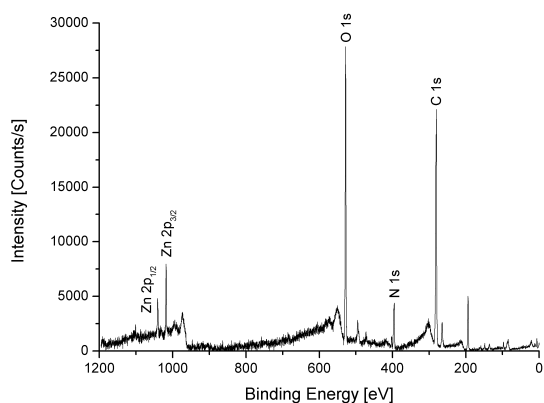


Figure 4: XPS spectrum (after charge correction and subtraction of an universal Tougaard background) recorded from an as-deposited precipitate containing peptide 31 (Deposition time: 4.5 h). The initial buffer solution had a pH of 7.5, which was obtained by adding NaOH solution.

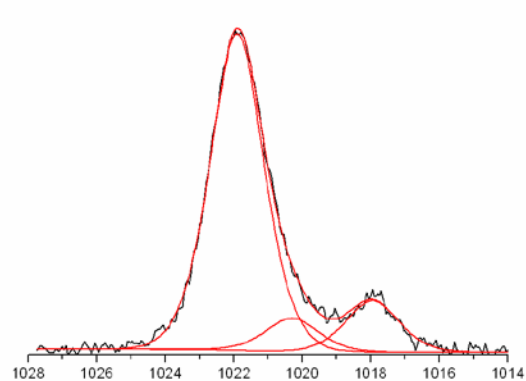


Figure 5: XPS spectrum of as-deposited precipitate containing peptide 31 (Deposition time: 4.5 h). The initial buffer solution had a pH of 7.5, which was obtained by adding NaOH solution.

Table 3: Binding Energies (BE; in eV) of the Zn $2p_{3/2}$ peak components as resolved by Constrained Peak Fitting of Charge-Corrected XPS spectra of the precipitates.

ZnO (Ref.)	Zn $2p_{3/2}$ BE (eV)			
		1021.9		
31	1021.9	1020.3	1018.0	
07	1021.9	1019.1		1016.2
46	1021.9	1019.6	1017.8	

Evidently, the XPS analysis confirms the incorporation of Zn, C, O, and N in all the studied precipitates; cf. the survey scan of peptide 31 in Figure 4. The measured Zn $2p_{3/2}$ region of the precipitates could be accurately fitted with up to four different main peaks, as positioned at (charge-corrected) BE values of $1021.9 \pm 0.1 \text{ eV}$, $1019.7 \pm 0.6 \text{ eV}$, $1017.9 \pm 0.1 \text{ eV}$ and 1016.2 eV (see Table 3). An exemplary spectral reconstruction of the Zn $2p_{3/2}$ region for peptide 31 is shown in Figure 4. The different local chemical states of the Zn ions in the precipitates, as evidenced by the

XPS analysis, are indicative of the presence of Zn ions in a mixed environment, as is the case for LBZs with a general formula $[(\text{Zn}^{\text{octa}})_3(\text{Zn}^{\text{tetra}})_2(\text{OH})_8]^{2+} \cdot 2(\text{A}^-) \cdot n\text{H}_2\text{O}$. Indeed the relative BE differences with respect to the Zn 2p_{3/2} main peak at 1021.9 ± 0.1 eV (as attributed to a ZnO-like local chemical environment) of 2.2 ± 0.2 eV, 4.0 ± 0.2 eV and 5.7 ± 0.2 eV are in accordance with the corresponding BE differences of the investigated LBZs in Gerstel et al. [14] (*note*: the absolute BE values differ due to the different charge-correction procedure applied in Ref. [14]). For the same reasons, the O 1s and N 1s regions are constituted of up to three main peaks: see Table 4. Finally, the measured C 1s region of the precipitates could be accurately fitted with either three or four main peaks, as attributed due to the presence of peptides within the LBZs and surficial adventitious carbon.

Table 4: Binding Energies (BE; in eV) of the O 1s, C 1s, and N 1s peak components (Corresponding to the resolved Zn 2p_{3/2} peak components in Table 3) as resolved by Constrained Peak Fitting of Charge-Corrected XPS Spectra of the precipitates.

	O1s BE (eV)			N1s BE (eV)			C1s BE (eV)			
ZnO (Ref.)	531.4	530.1		399.9	398.6		289.0	287.8	286.3	284.9
31		530.4	528.6	399.1	397.5	396.0	285.2	283.7	282.1	280.6
07	531.3			399.9	398.3		286.4	284.5	283.2	
46	531.5			399.6	397.9		287.7	285.9	284.5	

6-week experiments were carried out to investigate the precipitates in long-term experiments. Figure 6 shows representative XRD diagrams, which indicate, that the composition of precipitation has changed during precipitation time. Now, the characteristic (100)-, (002)- and (101)-reflections of the stable ZnO are the dominant reflections within the XRD diagrams.

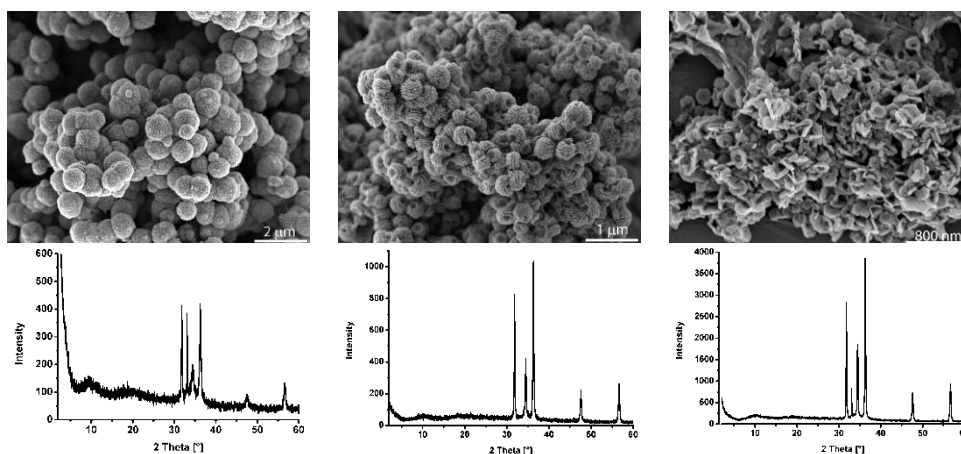


Figure 6: XRD diagrams and SEM figures of long-term experiments (6 weeks) with peptide 31, peptide 07 and peptide 46 (from left to right).

Table 5: Summary of the measured particle sizes (in nm) after a reaction time of 6 weeks at 37 °C.

Reflex	Control	Pep31	Pep07	Pep46
(100)	196	31	57	95
(002)	99	10	26	22
(101)	132	18	43	63
(002)/(100)	0.51	0.32	0.45	0.23

The disappearance of the other phases (α -hydroxide of zinc, LBZs) indicates that these phases are metastable intermediates. Thus the change of composition during time is in accordance with the Ostwald rule of stages, which is also valid within biomineralization processes [47].

Corresponding SEM micrographs of long-term experiments indicate the different morphologies of the precipitated ZnO (Figure 6). In the case of peptide 31, which has the highest relative binding strength in phage display experiment (cf. Table 5), characteristic globular aggregates with diameters of about 1 μm can be obtained. Peptide 46 produces hexagonal zinc oxide aggregates with typical holes in the centre. The diameter of these aggregates is in the range of about 100 to 300 nm. The precipitate in presence of peptide 07 features globular aggregates containing cavities at one pole side. The diameters are in the range of about 300 to 500 nm. Crystallite sizes within these aggregates were calculated using line-broadening analysis on the reflections with $hkl = (100)$, (002) and (101) . Table 5 shows the particle sizes of the precipitated particles. Due to the small ZnO particle sizes in presence of peptides it can be stated that ZnO-binding peptides inhibit the zinc oxide particle growth in comparison to the control experiment without peptides. A comparison of all particle sizes indicates an increasing binding affinity from peptide 46 to peptide 31. Furthermore, the different ZnO morphologies indicate a selective adsorption-growth inhibition mechanism during particle growth. The low particle size ratios of $(002)/(100)$ demonstrate the binding preference of the ZnO-binding peptides to the polar (001) -surface in comparison to the nonpolar (100) -surface.

Table 6: Modeled binding free energies (kcal mol^{-1}) for peptides binding to ZnO surfaces.

Surface	Pep31	Pep07	Pep46
(100)	8.5	6	5.4
(001)	39	19	14

Table 7: The binding sites of the peptides on the ZnO surfaces presented the highest binding free energy values.

Peptide	(001)-surface	(100)-surface
31	N-Ter, Arg12	Thr7, Ser8, Gln10
07	N-Ter, Arg9	His7, Thr12
46	N-Ter	Ser3

To model the preferred conformations of the three peptides binding to the O-terminated polar (001) or to the nonpolar (100) ZnO surfaces, their adsorption was simulated by three independent steered molecular dynamics simulations. For all three peptides, the positively charged side chains of arginine and the amino termini were identified as the dominant contacts between the peptides and the polar (001) -surface (Table 6). On the nonpolar (100) -surface, the uncharged side chains of threonine, serine, and glutamine, and the positively charged histidine were involved in binding. Thus, peptide binding to the polar and to the nonpolar surface is dominated by electrostatic interactions.

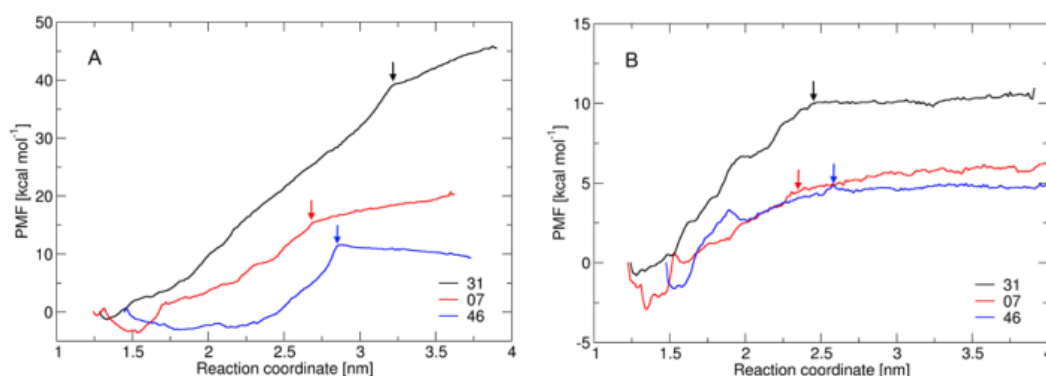


Figure 7: PMF curves for pulling the peptides 31 (black), 07 (red), and 46 (blue) from the ZnO (001) - (A) and (100) - (B) surfaces. The start of the plateau is indicated by an arrow.

To estimate the relative binding free energy for the three peptides towards the polar and the nonpolar ZnO surfaces, the PMF upon desorption of three binding conformations for each peptide was evaluated using a series of umbrella sampling simulations. For all peptides, the PMF profile had a similar shape: the peptide further relaxed as its centre of mass was moved by 1–1.5 nm away from the surface, then the PMF steeply increased as the contacts between the anchoring residues and the surface were lost (Figure 7). It ended in a plateau with a constant slope that depended only on the charge of the peptide. The plateau region started between 2.7 and 3.2 nm for the (001)-surfaces and at 2.5 nm for the (100)-surface. The free energy difference between the minimum at 1–1.5 nm and the start of the plateau region was taken as the binding free energy. It depended sensitively on the binding conformation: at the polar (001)-surface 40.5, 22.0 and 18.5 kcal mol⁻¹ for peptide 31, 19.0, 18.0 and 17.0 kcal mol⁻¹ for peptide 07, and 14.0, 10.3 and 9.2 kcal mol⁻¹ for peptide 46; at the nonpolar (100)-surface 10.2, 3.4 and 3.2 kcal mol⁻¹ for peptide 31, 6.0, 4.0 and 3.0 kcal mol⁻¹ for peptide 07 and 5.4, 4.0 and 1.5 kcal mol⁻¹ for peptide 46. The highest binding free energy for each peptide and each surface was selected as a measure of the ZnO binding affinity (Figure 7). Peptide 31 had the highest binding energies toward both surfaces (40.5 and 10.2 kcal mol⁻¹ toward the polar and the nonpolar surface, respectively), while peptide 07 (19.0 and 6.0 kcal mol⁻¹, respectively) and peptide 46 (14.0 and 5.4 kcal mol⁻¹, respectively) showed considerably lower binding energies. All three peptides had a different number of peptide-ZnO contacts, which were selected based on the initial structures of the desorption simulations of each peptide on each surface, but the numbers of peptide contacts were not correlated to their simulated binding free energies (Table 7). The conclusions from the relative binding free energy analysis agree with previous experimental observations that peptide 31 is by far a better ZnO binder than peptides 07 and 46 [25].

Binding of a peptide to the ZnO crystal surface has been suggested to inhibit the growth of the ZnO particle by reducing the surface energy [48]. Selective binding to one of the surfaces is expected to reduce the growth in the respective direction while increasing growth in on other directions. Thus, the aspect ratio of the resulting ZnO particle is modified. In fact, direct experimental evidence of peptides controlling the ZnO particle morphology has been reported [18,21].

The modeled binding energies of the three peptides toward the polar and the nonpolar surfaces were in accordance with the observed decrease of ZnO particle size perpendicular to the polar and nonpolar surface. The best binder as determined by modeling, peptide 31, considerably inhibited the growth of ZnO in comparison with the control without added peptide, according to the measurement of particle size distribution of ZnO after 6 weeks of the reaction (Table 5), by a factor of 9.9 and 6.3 toward the polar and nonpolar surfaces, respectively. The two medium binder peptides 07 and 46 also bound to the polar surface and decreased the ZnO particle size, however at a lower degree, by a factor of 3.8 (peptide 07) and 4.5 (peptide 46), and toward the nonpolar surface by a factor of 3.4 (peptide 07) and 2.1 (peptide 46).

Thus, the peptide-mediated changes of the shape of the crystals and the observed shift in the aspect ratio could be explained by a quantitative model of peptide binding. However, the size and morphology of the precipitates might be influenced by additional physical and chemical factors associated with the ZnO-binding peptides [12,18,21,49,50], thus leading to slight deviations between the aspect ratio of the precipitates and the ratio between the evaluated binding energies.

4. CONCLUSIONS

Zinc oxide crystals have been synthesized under moderate conditions in presence of three different ZnO-binding 12-mer peptides, which have isoelectric points in the acidic, near neutral and basic pH

range, respectively. From XRD and FTIR investigations, it was established that negatively charged peptides intercalate easily in metastable LBZs. Additionally, the α -hydroxide of zinc can be identified as a second metastable phase. During the reaction time the metastable phases disappear and stable zinc oxide is favoured. Thus, the Ostwald rule of stages is the key for understanding the precipitation mechanism under bio-inspired conditions.

Furthermore, it can be concluded that ZnO-binding peptides inhibit the particle growth of ZnO crystals, which results in smaller zinc oxide crystal sizes in comparison to reference experiments without ZnO-binding peptides. The inhibition behavior of peptides is in accordance with modeling calculations. Although we do not have enough experimental data to describe the ZnO growth process entirely, it is interesting to note that the binding free energy from computer simulations seems to be correlated with the current experiment results of the bio-inspired particle formation of ZnO via the binding of the peptides.

5. ACKNOWLEDGMENT

We are grateful for financial support provided by the Deutsche Forschungsgemeinschaft (BI 469/15-1 and PL145/8-1) within the scope of the project "Biologische Erzeugung von Oxidkeramiken" (PAK 410). The help of M. Wieland, M. Dudek (both MPI-IS) and W. König (MPI-FKF) with the XPS, XRD and FTIR measurements, respectively, is gratefully acknowledged. Dipl.-Ing. T. Lehmann is thanked for TGA measurements. Prof. Dr. P. A. van Aken (MPI-IS) is thanked for providing the SEM.

6. REFERENCES

- [1] Pearton S. J., Norton D. P., Ip K., Heo Y. W., Steiner T., Recent progress in processing and properties of ZnO, *Progress Mater Sci.* 50, 293-340, **2007**.
- [2] Oh B. Y., Jeong M. C., Moon T. H., Lee W., Myoung J. M., Hwang J. Y., Seo D. S., Transparent conductive Al-doped ZnO films for liquid crystal displays, *J. Appl. Phys.* 99, 124505, **2006**.
- [3] Chopra K. L., Major S., Pandya D. K., Transparent conductors - A status report, *Thin Solid Films* 102, 1-46, **1983**.
- [4] Leary D. J., Barnes J. O., Jordan A. G., Calculation of carrier concentration in polycrystalline films as a function of surface acceptor state density: application for ZnO gas sensors, *J. Electrochem. Soc.* 129, 1382-1386, **1982**.
- [5] Klingshirn C. F., Meyer B. K., Waag A., Hoffmann A., Geurts J., *Zinc Oxide: From Fundamental Properties Towards Novel Applications*, Springer, **2010**.
- [6] Newman S. P., Jones W., Comparative Study of Some Layered Hydroxide Salts Containing Exchangeable Interlayer Anions, *J. Solid State Chem.* 148, 26-40, **1999**.
- [7] Wypych F., Arizaga G. G. C., Gardolinski J. E. F. D., Intercalation and functionalization of zinc hydroxide nitrate with mono- and dicarboxylic acids, *J. Colloid Interface Sci.* 283, 130-138, **2005**.
- [8] Arizaga G. G. C., Satyanarayana K. G., Wypych F., Layered hydroxide salts: Synthesis, properties and potential applications, *Solid State Ionics* 178, 1143-1162, **2007**.
- [9] Arizaga G. G. C., Mangrich A. S., Gardolinski J. E. F. d. C., Wypych F., Chemical modification of zinc hydroxide nitrate and Zn-Al-layered double hydroxide with dicarboxylic acids, *J. Colloid Interface Sci.* 320, 168-176, **2008**.
- [10] Arizaga G. G. C., Gardolinski J. E. F. d. C., Schreiner W. H., Wypych F., Intercalation of an oxalatoxonioabate complex into layered double hydroxide and layered zinc hydroxide nitrate, *J. Colloid Interface Sci.* 330, 352-358, **2009**.
- [11] Cordeiro C. S., Arizaga G. G. C., Ramos L. P., Wypych F., A new zinc hydroxide nitrate heterogeneous catalyst for the esterification of free fatty acids and the transesterification of vegetable oils, *Catal. Commun.* 9, 2140-2143, **2008**.
- [12] Umetsu M., Mizuta M., Tsumoto K., Ohara S., Takami S., Watanabe H., Kumagai I., Adschiri T., *Adv. Mater.* 17, 2571-2575, **2005**.

- [13] Gerstel P., Lipowsky P., Durupthy O., Hoffmann R. C., Bellina P., Bill J., Aldinger F., Depositopn of Zinc Oxide and Basic Zinc Salts from Aqueous Solutions Containing Amion Acids and Dipeptides, *J. Ceram. Soc. Japan* 114, 911-917, **2006**.
- [14] Gerstel P., Hoffmann R. C., Lipowsky P., Jeurgens L. P. H., Bill J., Aldinger F., Mineralization from Aqueous Solutions of Zinc Salts Directed by Amino Acids and Peptides, *Chem. Mater.* 18, 179-186, **2006**.
- [15] Bauermann L. P., Bill J., Aldinger F., Bio-friendly Synthesis of ZnO Nanoparticles in Aqueous Solution at Near-Neutral pH and Low Temperature, *J. Phys. Chem.* 110, 5182-5185, **2006**.
- [16] Bauermann L. P., Bill J., Aldinger F., Bio-inspired syntheses of ZnO-protein composites, *Int. J. Mat. Res.* 98, 879-883, **2007**.
- [17] Dickerson M. B., Sandhage K. H., Naik R. R.; Protein and Peptide directed synthesis of inorganic materials, *Chem. Rev.* 108, 4935-4978, **2008**.
- [18] Tomczak M. M., Gupta M. K., Drummy L. F., Rozenzhak S. M., Naik R. R.; Morphological control and assembly of zinc oxide using a biotemplate, *Acta Biomater.* 5, 876-882, **2009**.
- [19] Chen C.-L., Rosi N. L., Peptide-Based Methods for the Preparation of Nanostructured Inorganic Materials, *Angew. Chem. Int. Ed.* 49, 1924-1942, **2010**.
- [20] Togashi T., Yokoo N., Umetsu M., Ohara S., Naka T., Takami S., Abe H., Kumagai I., Adschiri T., Material-binding peptide application-ZnO crystal structure control by means of a ZnO-binding peptide, *J. Biosci. Bioeng.*, 111, 140-145, **2011**.
- [21] Liang M.-K., Deschaume O., Patwardhan S. V., Perry C. C., Direct evidence of ZnO morphology modification *via* the selective adsorption of ZnO-binding peptides, *J. Mat. Chem.*, 21, 80-89, **2011**.
- [22] Baier J., Strumberger R., Berger F., Atanasova P., Welzel U., Bill J., Mineralization and particle growth kinetics of ZnO in zhe presence of gelatin, *Biointerfâce Res. Appl. Chem.*, 2, 339-349, **2012**.
- [23] Kornherr A., Hansal S., Hansal W. E. G., Besenhard J. O., Kronberger H., Nauer G. E., Zifferer G., Molecular dynamics simulations of the adsorption of industrial relevant silane molecules at a zinc oxide surface, *J. Chem. Phys.* 119, 9719-9728, **2003**.
- [24] Kornherr A., French S. A., Sokol A. A., Catlow C. R. A., Hansal S., Hansal W. E. G., Besenhard J. O., Kronberger H., Nauer G. E., Zifferer G., Interaction of adsorbed organosilanes with polar zinc oxide surfaces: a molecular dynamics study comparing two models for the metal oxide surface, *Chem. Phys. Lett.*, 393, 107-111, **2004**.
- [25] Kornherr A., Hansal S., Hansal W. E. G., Nauer G. E., Zifferer G., Molecular Dynamics Simulations of the First Steps of the Formation of Polysiloxane Layers at a Zinc Oxide Surface, *Macromol. Symp.* 217, 295-300, **2004**.
- [26] Rothenstein D., Claasen B., Omiecienski B., Lammel P., Bill J., Isolating of ZnO-binding 12-mer peptides and determination of their binding epitopes by NMR spectroscopy, *J. Am. Chem. Soc.*, in press.
- [27] DeKeijser T. H., Langford J., Mittemeijer E. J., Vogels A. B. P. J., Use of the Voigt function in a single-line method for the analysis of X-ray diffraction line broadening, *Appl. Crystallogr.*, 15, 308-314, **1982**.
- [28] Mittemeijer E. J., Welzel U., The „state of the art“ of the diffractiob analysis of crystallite size and lattice strain, *Z. Kristall.* 223, 552-560, **2008**.
- [29] Vinodh M. S., Jeurgens L. P. H., Quantitative analysis of angle-resolved XPS spectra recorded in parallel data acquisition mode, *Surface and Interface Analysis*, 36, 1629-1636, **2004**.
- [30] Van der Spoel D., Lindahl E., Hess B., Groenhof G., Mark A. E., Berendsen H. J. C., GROMACS: Fast, flexible, and free, *J. Comput. Chem.*, 26, 1701-1718, **2005**.
- [31] Weiner S. J., Kollmann P. A., Case D. A., Singh U. C., Ghio C., Alagona G., Profeta S., Weiner, P., A new force field for molecular mechanical simulation of nucleic acids and proteins, *J. Am. Chem. Soc.*, 106, 765-784, **1984**.
- [32] Duan Y., Wu C., Chowdhury S., Lee M. C., Xiong G. M., Zhang W., Yang R., Cieplak P., Luo R., Lee T., Caldwell, J., Wang J. M., Kollman P., A point-charge force field for molecular mechanics simulations of proteins based on condensed-phase quantum mechanical calculations, *J. Comput. Chem.*, 24, 1999-2012, **2003**.
- [33] Xu Y. N., Ching W. Y., Electronic, optical, and structural properties of some wurtzite crystals, *Phys. Rev. B*, 48, 4335-4351, **1993**.
- [34] Kumar S., Bouzida D., Swendsen R. H., Kollman P. A., Rosenberg J. M., THE weighted histogram analysis method for free-energy calculations on biomolecules. I. The method, *J. Comput. Chem.*, 13, 1011-1021, **1992**.
- [35] Pelton J. T., McLean L. R., Spectroscopic Methods for Analysis of Protein Secondary Structure, *Anal. Biochem.*, 277, 167-176, **2000**.

- [36] Brandes N., Welzel P. B., Werner C., Kroh L. W., Adsorption-induced conformational changes of proteins onto ceramic particles: Differential scanning calorimetry and FTIR analysis, *J. Colloid Interface Sci.*, 299, 56-69, **2006**.
- [37] Stoilova D., Koleva V., Vassileva V., Infrared study of some synthetic phases of malachite ($\text{Cu}_2(\text{OH})_2\text{CO}_3$)-hydrozincite ($\text{Zn}_5(\text{OH})_6(\text{CO}_3)_2$) series., *Spectrochim. Acta, Part A*, 58, 2051-2059, **2002**.
- [38] Hales M. C., Frost R. L., Synthesis and vibrational spectroscopic characterisation of synthetic hydrozincite and smithsonite, *Polyhedron*, 26, 4955-4962, **2007**.
- [39] Hibino T., Delamination of Layered Double Hydroxides Containing Amino Acids, *Chem. Mater.*, 16, 5482-5488, **2004**.
- [40] Feitknecht W., Über die α -Form der Hydroxide zweiwertiger Metalle, *Helv. Chim. Acta*, 21, 766-784, **1938**.
- [41] Yang J.-H., Han Y.-S., Park M., Park T., Hwang S.-J., Choy J.-H., New Inorganic-Based Drug Delivery System of Indole-3-Acetic Acid-Layered Metal Hydroxide Nanohybrids with Controlled Release Rate, *Chem. Mater.*, 19, 2679-2685, **2004**.
- [42] Hussein M. Z., Bahar F. A., Yahaya A. H., Synthesis and Characterisation of Hippurate-Layered Double Hydroxide Nanohybrids and Investigations of its Release Property, *J. Iran Chem. Soc.*, 7, S42-S51, **2010**.
- [43] Hosono E., Fujihara S., Honma I., Zhou H., The Fabrication of an Upright-Standing Zinc Oxide Nanosheet for Use in Dye-Sensitized Solar Cells, *Adv. Mater.*, 17, 2091-2094, **2005**.
- [44] Bitenc M., Podbršček P., Dubček P., Bernstorff S., Dražić G., Orel B., Pejovnik S., Orel Z. C., The growth mechanism of zinc oxide and hydrozincite: a study using electron microscopies and *in situ* SAXS, *Chem. Eur. J.*, 16, 11481-11488, **2010**.
- [45] Feitknecht W., Laminardisperse Hydroxyde und basische Salze zweiwertiger Metalle, *Colloid. Polym. Sci.*, 93, 66-86, **1940**.
- [46] Cavani F., Trifiro F., Vaccari A., Hydrocalcite-type anionic clays: preparation, properties and applications, *Catal. Today*, 11, 173-301, **1991**.
- [47] Mann S., *Biomineralization*, Oxford University Press, **2005**.
- [48] Muthukumar M., Theory of competitive adsorption-nucleation in polypeptide-mediated biomineralization, *J. Chem. Phys.*, 130, 161101-161105, **2009**.
- [49] Meulenkamp E. A., Synthesis and Growth of ZnO Nanoparticles, *J. Phys. Chem.*, 102, 5566-5572, **1998**.
- [50] Shen Q., Gao Y. -F., Miao H. -Y., Luo H. -J., Nagai M., Influence of soluble polymers on the formation of ZnO films from aqueous solutions, *Thin Solid Films*, 518, E16-E23, **2010**.